HHS Public Access

Author manuscript

IEEE Trans Biomed Eng. Author manuscript; available in PMC 2017 September 01.

Published in final edited form as:

IEEE Trans Biomed Eng. 2017 July ; 64(7): 1535–1546. doi:10.1109/TBME.2016.2612541.

Automated Compression Device for Viscoelasticity Imaging

Alireza Nabavizadeh[1,2], **Randall R. Kinnick**[2], **Mahdi Bayat**[2] **[Member, IEEE]**, **Carolina Amador**[2], **Matthew W. Urban**[2,3] **[Senior Member, IEEE]**, **Azra Alizad**[2,3] **[Senior Member, IEEE]**, and **Mostafa Fatemi**[2] **[Fellow IEEE]**

[1]Biomedical Informatics and Computational Biology, University of Minnesota Rochester, Rochester, Minnesota, USA

[2]Department of Physiology and Biomedical Engineering, Mayo Clinic College of Medicine, Rochester, Minnesota, USA

[3]Department of Radiology, Mayo Clinic College of Medicine, Rochester, Minnesota, USA

Abstract

Non-invasive measurement of tissue viscoelastic properties is gaining more attention for screening and diagnostic purposes. Recently, measuring dynamic response of tissue under a constant force has been studied for estimation of tissue viscoelastic properties in terms of retardation times. The essential part of such a test is an instrument that is capable of creating a controlled axial force and is suitable for clinical applications. Such a device should be lightweight, portable and easy to use for patient studies to capture tissue dynamics under external stress. In this paper we present the design of an automated compression device for studying the creep response of materials with tissue-like behaviors. The device can be used to apply a ramp-and-hold force excitation for a predetermined duration of time and it houses an ultrasound probe for monitoring the creep response of the underlying tissue. To validate the performance of the device, several creep tests were performed on tissue-mimicking phantoms and the results were compared against those from a commercial mechanical testing instrument. Using a second order Kelvin-Voigt model and surface measurement of the forces and displacements, retardation times T_1 and T_2 were estimated from each test. These tests showed strong agreement between our automated compression device and the commercial mechanical testing system, with an average relative error of 2.9% and 12.4 %, for T_1 and T_2 respectively. Also, we present the application of compression device to measure local retardation times for four different phantoms with different size and stiffness.

Keywords

creep response; retardation time; ultrasound; viscoelasticity

I. Introduction

Mechanical properties of a medium can be assessed by different mechanical testing methods. These methods cover a large range of conventional mechanical testing techniques

Correspondence: nabav005@umn.edu.

like indentation [1,2,3] shear rheology [5], compression testing [6], uniaxial tensile testing [7], magnetic force methods [8], and bulge tests [9].

Elastography is a modality for evaluating the stiffness in tissue. This method can provide an insight about the local mechanical properties of the medium when it is combined with other imaging modalities like ultrasound [10, 11] or magnetic resonance imaging (MRI) [12].

Based on the excitation source, elastography techniques can be divided in two main subgroups: dynamic elastography which is based on dynamic force stimulus [11, 13, 14, 15] and quasi-static strain elastography in which a compressive force is applied [10]. Both the dynamic and quasi-static elastography techniques have been implemented on ultrasound imaging systems. Shear wave elastography is a dynamic elastography method in which the elasticity is estimated based on the shear wave induced by an excitation. The excitation may be from an external source [16], or an internal source, such as acoustic radiation force. Several techniques have been developed based on the acoustic radiation force, including Supersonic Shear Imaging (SSI) methods [13], Acoustic Radiation Force Impulse (ARFI) [14], and Shear Wave Dispersion Ultrasonic Vibrometry, SDUV [17]. These shear wave elastography methods have been applied to conduct *in vivo* studies in liver [18,19], thyroid [22, 23], prostate [24] and breast [20,21,25]. Among these shear wave elastography methods, SSI, SDUV, and ARFI have been used to quantify the viscoelastic properties of the soft tissue.[17,25, 26].

In strain elastography the strain map is created by compressing the tissue and recording the pre- and post-compression displacement profiles [10, 27]. The strain is lower in a stiffer material than in a softer material. Because it is not possible to measure a local distribution of stress, one cannot measure the quantitative values of stiffness or the Young's modulus in this method [10, 27]. Therefore, relative changes in the strain within the image have been used to detect various anomalies in different organs like breast [28, 29, 30], prostate [31], thyroid [32].

Creep test is a dynamic viscoelasticity imaging [33], in which a step force is applied on the object for a relatively long time, and the strain behavior of the tissue is recorded during the impression period.

It is common to use a rheological model to evaluate the viscoelastic response of the medium. These models are used to show the relationship between the stress and strain that models the viscoelastic response of tissue and its structure. The standard rheological models like, Maxwell [33], Kelvin-Voigt model [33, 34, 35, 36] and standard linear solid models [33] are the most applicable ones. Sloninsky, *et al.* [37] described a model called fractional derivative to model the behavior of biological tissue with lower number of fit parameters [38].

Viscoelastic mechanical properties have been linked to pathology of soft tissue [39, 40, 41]. An explanation for this is the alteration of the extracellular matrix in diseased tissues, which can manifest as changes in tissue mechanical properties [42, 43]. It has been shown that the mechanical behavior of the collagen has the main role in viscoelastic response not only in hydrogel phantoms [15,44] but also in tissues such as lung [45], liver [46], prostate [47], skin [48], uterus [49] and breast [50]. Qiu, *et al.* [51] showed that it is possible to

differentiate between the nonpalpable malignant and benign tumor in patients based on their viscoelastic creep response.

Shear wave elastography and creep test method measure the mechanical properties of tissue at different time and frequency scales, which may affect their outcome. Shear wave elastography measures the elasticity at high frequency range in the order of hundreds of Hertz and during a short time period. The creep test, on the other hand, measures the viscoelasticity of tissue over a long time period, in the order of seconds, which corresponds to the frequency range of less than a Hertz [52].

Employing the creep test in different imaging modalities like ultrasound [50, 51], MRI [53, 54] to evaluate the viscoelastic properties of the medium has been proposed by a number of investigators. For this purpose, compression devices have been designed for such imaging modalities [42, 53]. Other investigators [54–61] have proposed various compression devices for elasticity imaging, where such devices are mainly designed for testing tissue at its rest position after the compression. Tissue compression has been also investigated in the context of poroelasticity [62–65]. However, these studies aimed at measuring stress relaxation response of the medium.

Hand-held compression method has been discussed in [50, 51] for *in vivo* creep test employing ultrasound imaging. However, manual compression is usually accompanied with noise due to hand jitter, which may reduce the reproducibility and repeatability of this method [50].

In this paper, we are interested in the viscoelastic response of the tissue, for which we need to study the temporal response of tissue under a constant stress.

The goal of this study is to design and validate a fully automatic device with the ability to apply an approximate step force to excite the viscoelastic creep response in tissue while allowing *in vivo* ultrasound image acquisition during the transient response of tissue. To validate the device we will compare its performance with a standard mechanical testing device and measure the related error. The long-term goal of this study is to employ this device to conduct creep test on a group of breast patients. Previously, creep test studies of human breast have been conducted using manual compression [50,51].

The remainder of this paper is organized as follows. In section two, we provide an overview of the rheological techniques for modeling tissue deformations under creep-like tests and highlight the hardware requirements for performing such tests. In section three, we explain the details of the compression device that is specifically designed to apply step-like stress on tissue. In the next section, the function of this device is validated by comparing its results with those of a standard mechanical testing instrument [59], using tissue-mimicking samples [42, 44, 50, 66, 67]. Section five is devoted to integration of the compression device with a programmable ultrasound machine for viscoelasticity imaging based on ultrasound strain estimation. We discuss the results of the validation tests as well as viscoelasticity imaging in section six. The paper concludes with a brief summary of the results and future applications of the device.

II. Methods

A. Creep Response of Material

Under an external stress, material deformation can be modeled using the constitutive equations from continuum mechanics. Simplified models such as the generalized Kelvin-Voigt model are shown to be suitable in the case of uniaxial constant stress on hydrogels and their creep responses are shown to be close to those of soft tissue [44].

For each point inside the material the strain-stress relationship is

$$\varepsilon(t)=\int_{t_0}^{t} dtD(t-\tau)\frac{d\sigma(t)}{dt} \quad (1)$$

where $\sigma(t)$ is the stress applied at $t = t_0$, $D(t)$ the creep compliance and $\varepsilon(t)$ is the resulting strain [33, 50]. For generalized Kelvin-Voigt model with an added elastic term, the creep compliance may be expanded as

$$D(t)=\frac{1}{E_0}+\sum_{r=1}^{n}\frac{1}{E_r}\left(1-e^{-\frac{t}{T_r}}\right) \quad (2)$$

where E_0 represents the pure elastic part, η_r and E_r are the viscosity and elasticity coefficients and $T_r = \eta_r/E_r$ is the r^{th} retardation time [22]. In the creep test the stress applied at $t = t_0$ can be modeled as

$$\sigma(t)=\sigma_0 u(t-t_0) \quad (3)$$

where $u(t)$is the Heaviside function and σ_0 is the constant stress.

Using (2) in (1) with applying the input stress as defined in (3) the general creep response can be written as

$$\varepsilon(t)=\varepsilon_0+\sum_{r=1}^{n}\varepsilon_r\left(1-e^{-\frac{(t-t_0)}{T_r}}\right) \quad (4)$$

where $\varepsilon_0 = \sigma_0 u(t - t_0)\ E_0$ is the initial elastic response and $\varepsilon_r = \sigma_0/E_r$ is the amplitude of the contribution of the r^{th} viscoelastic term.

The number of exponential terms, n, depends on the complexity of the material and the observation time scale. For example, a second order Kelvin-Voigt model was in [10] used to analyze only the creep response of tissue. In the present study, we will use a second-order Kelvin-Voigt rheological model to model the creep response as

$$\varepsilon(t)=\varepsilon_1(1-\exp(-\tfrac{t}{T_1}))+\varepsilon_2(1-\exp(-\tfrac{t}{T_2})) \quad (5)$$

Equation (5) models the response in terms of two retardation times T_1 and T_2 and the corresponding amplitudes ε_1 and ε_2, respectively, without considering the initial elastic term.

In practice, it is not possible to apply a step force and study its response. It is, however, possible to approximate the step force with a ramp-and-hold force, where the speed of the ramp is adjusted to suit the response of the material under test. The ramp speed should be chosen fast enough such that the initial elastic response of material can be easily separated from the slow creep response [68].

B. System Design

In almost all commercial mechanical testing machines, the theoretical step stress required for the creep test is replaced by a highly controlled ramp function. However, the speed of such ramp stress should be high enough to be able to capture the shortest retardation times of the material under the test. The aim of this work is to design a compression device that is able to create such ramp forces with the additional feature of housing an ultrasound probe for continuous strain imaging during the test.

A schematic of the device is shown in Figure 1. This device is equipped with an ultrasound probe which can record the local deformation of tissue under stress. This device consists of a lightweight, miniature linear actuator, (MR20LS with 2 mm lead screw, PBC Linear, Roscoe, IL), driven by a brushless DC (BLDC) servomotor, (RP17M brushless DC servomotor with encoder, Electrocraft, Dover, NH) which moves a commercial ultrasound probe together with a back and pressure plate rapidly onto the material or tissue until a preset force level on the pressure plate is reached. The encoder associated with the motor measures the displacement of the pressure plate. The actuator control system uses 4 small load sensors (FSS015, 15 Newton range, Honeywell, Bloomington, MN), embedded in a back plate, to measure the applied force. The control system maintains the preset force level constant for a predetermined period of time, typically about 10–100 seconds. When the creep response measurement is complete, the actuator automatically retracts the probe.

The back plate is custom fit to the probe using a liquid castable plastic material (SmoothCast 300, Smooth-on, Inc., Easton, PA). The four small load sensors are sandwiched between the back plate and the pressure plate. Figure 2 shows the position of the load sensors at the four corners of the back plate. Thus, as the motor is applying the compression on an object, the resulting resisting force from the object is transferred to the load sensors by the pressure plate.

There is a rectangular hole (acoustic window) at the center of the pressure plate. The probe face is placed such that the ultrasound can pass through this acoustic window. The outside surface of this hole (the side that is toward the object) is covered by a thin, acoustically transparent, membrane. There is a small gap between the probe surface and the thin

membrane, where this gap is filled with acoustic gel (almost a liquid). When the pressure plate is pressed against the object, the gel-filled gap prevents the transfer of stress onto the probe surface (although a small amount of gel may be pushed out of the gap due to slight bulging of the membrane). That is, the pressure will not act on the probe surface. Therefore, the forces measured by the 4 sensors are the cumulative force acting on the pressure plate and the attached membrane. The overall dimensions of the device is 31 cm × 7 cm × 5.5 cm (length × width × depth).

Since the ultimate application of this compression device is in breast patients the optimal range of applied force would be less than 20 seconds. The device is attached to a platform, which is held by an articulated arm. This way there is no need manual handling of the compression device thus avoiding possible hand motions.

III. Experimental studies

Validation of the Automated Compression Device

A. Force measurement—In order to validate the compression device for performing material creep test, we used a standard mechanical testing instrument (Bose ElectroForce®, Eden Prairie, MN) [49] to apply force and record the resulting displacement and repeated the same procedure with automated compression device, then compared the results. We used a forcing function in the form of ramp-and-hold with 3 N final force and 18 N/s ramp rate (ramp duration of 1/6 seconds). We experimentally determined that 18 N/s ramp is the maximum ramp speed that we can use without any ringing effects for the gelatin phantoms used in our experiments. Figure 3 shows the simplified schematic of the Bose mechanical testing instrument.

Creep tests were performed on a homogenous tissue-mimicking phantom. To construct the phantom 13.7 grams gelatin (Sigma-Aldrich, St. Louis, MO), 60 mL Vanicream Lite (Pharmaceutical Specialties, Inc., Rochester, MN), 0.3 grams of agar (A5306, Sigma-Aldrich), 3 grams cellulose (Sigma-Aldrich) for ultrasound scattering and 3 grams potassium sorbate (Sigma-Aldrich) as a preservative, were dissolved in enough water to make the total solution volume equal 300 mL. The phantom was made at room temperature and kept one day before using it for experiment. The phantom dimensions were 4×6×2 cm (length × width × height). The recipe used for our phantom is close to the one used in previous studies [66, 67] for making a viscoelastic phantom.

We tested the same phantom with our compression device and with the Bose system at identical force and ramp functions. The surface displacement data resulting from Bose system and the compression device outputs were recorded for 85 seconds.

It should be noted that phantom dimensions are smaller than the pressure plate of the compression device and also smaller than the plate of the Bose instrument; therefore, the compression is applied similarly on the entire top surface of the phantom in both cases. In either system, the bottom surface of the phantom rests on a platform, where free slip boundary condition is assumed. This allows for minimal boundary condition effects and thus the results would be comparable for both devices. Figure 4 illustrates the load (force sensor

output) from our compression device and the Bose instrument at force level of 3 N with 18 N/s ramp speed. Figure 4(a) shows the entire force signal. Fig. 4(b) displays only the initial 10 seconds for better visualization. Both devices reach their final force values in a fraction of second.

B. Displacement Measurement and Retardation Time Estimation—To validate the compression device performance, we measured the retardation times of a test phantom by the both compression device and the Bose instrument, and the outcomes were compared. For this purpose, we measured the surface displacement of the phantom.

Because the applied force is not a pure step function, the initial part of the response is a complicated mixture of the elastic and viscoelastic responses to the ramp excitation. However, after the force reaches its final value, it is safe to assume that the time varying part of the strain profile is only due to viscoelastic response. For this reason, the initial 1 second part of the response is excluded from the strain data analysis and the model is reduced to a second order Kelvin-Voigt model, Eq. (5) [63, 69].

Figure 5 illustrates the surface displacement profile resulted from the Bose instrument and our compression device before and after fitting a curve according to Eq. (5). A nonlinear least squares optimization method was used to find the closest fit to measure the two retardation times T_1 and T_2.

C. Model Fitting Evaluation—In order to evaluate the suitability of the Kelvin-Voigt model for observed slow creep deformations, as shown in Eq. (5), it is necessary to quantify the amount of deviation from this model. The measured strain at a discrete time point t_n, n =1,2,…N, can be modeled as

$$\hat{d}(t_n)=d_f(t_n)+e(t_n) \quad (6)$$

where $\hat{d}(t_n)$ is the measured strain and $d_f(t_n)$ represents the fitted viscoelastic compliance curve based on the selected model. $e(t_n)$ represents the residual error.

A normalized error can then be introduced as expressed in Eq. (7), where Q quantifies the goodness of the fit in terms of the power of residual error, $e(t_n)$, relative to the power of the total measured strain

$$Q=\sqrt{\frac{\frac{\sum_{n=1}^{N}(\hat{d}(t_n)-d_f(t_n))^2}{N}}{\frac{\sum_{n=1}^{N}\hat{d}(t_n)^2}{N}}}*100 \quad (7)$$

Such error measure has the advantage that model deviation can be quantified regardless of the total strain value.

Applying Eq. (7) on the displacement data in Figure 5 results in Q = 0.52% error for Bose instrument response and Q = 0.86% for the compression device response.

To test measurement reproducibility, we repeated these experiments five times on the same phantom using the same force, 3 N, and ramp speed, 18 N/s. Table 1 shows the resulting T_1 and T_2 values for these measurements.

In order to compare the results of the two devices, a relative error for each parameter is defined as follows

$$E(\%)=\frac{T_D-T_B}{T_B}*100 \quad (8)$$

In this equation (T_D) is the retardation time, T_1 or T_2, measured by the compression device and (T_B) is corresponding values measured by the Bose machine, which is regarded as the gold standard. Based on the average results of 5 trials, the error percentage, *E(%),* for T_1 and T_2 were − 2.9% and −12.4%, respectively. These results indicate a strong agreement between the creep device and Bose instrument. We used t-test to compare the results of the compression device and the BOSE machine. The t-test showed a p-value of 0.4 which proves that there is no significance difference between two devices.

We did not repeat the test on phantoms more than 10 times, 5 times for BOSE machine and 5 times for compression device, because there was a risk of damaging the phantom.

D. Retardation Time Imaging—In this section we present the application of the compression device combined with ultrasound strain imaging for viscoelasticity evaluation of a medium. The first step in retardation time imaging is acquiring sequential IQ data of the phantom that is being compressed by the compression device. Next, these data are used to calculate the strain at every pixel. Then, the retardation time at each pixel is estimated to produce an image depicting the retardation time distribution across the phantom.

Figure 6 shows the block diagram of the ultrasound probe pressure plate and the location of the phantom

The phantom used for this experiment is the same one that was used in Section A. We used the compression device to apply a 3 N force with 18 N/s ramp. An ultrasound system (Verasonics, Inc., Kirkland, WA, USA) with a linear array transducer (L11–4v, Verasonics, Inc., Kirkland, WA, USA) was used to monitor the phantom response. For this purpose, we used plane wave mode [70] to acquire a series of RF data of the phantom during the compression. Figure 7 shows the first B-mode image from the acquisition sequence. In this experiment, the ultrasound center frequency was 6.43 MHz and the frame rate was 20 Hz during the acquisition time of 85 seconds; thus, 1700 frames were acquired.

E. Displacement and strain calculation—A two-dimensional autocorrelation method was used to calculate the particle velocity from adjacent frames and then the displacements were estimated by integrating the particle velocity in time [71].

After calculating the displacement for all consecutive IQ data, the corresponding strain values were computed based on the gradient of the displacement. An axial 20 λ window was defined to measure the strain followed by a moving average filter with 1.2×1.2 mm size. The total strain map and the strain profiles are shown in Fig. 8. Figure 8(a) shows the spatial distribution of the total strain. Fig. 8(b) depicts the strain profiles for the locations specified in (a). The strain profiles with standard deviation related to point 1 and 5 specified in (a) is shown figure 8(c). Then all of the strain curves were normalized and shown in Fig. 8(d). Also included in this figure is the normalized surface displacement, which can be regarded as the overall strain behavior. As it can be seen, the normalized strain profiles from different points show similar dynamics. It is also observed that the dynamic behaviors of these points closely match that of the normalized surface displacement even though the total strain values are different. The spatial variations of the strain, as seen in Figs. 8(a) and (b), is related to the geometry and the boundary conditions of the medium, a phenomenon that has been discussed in many studies [72, 73, 74, 75].

F. Two Dimensional Visualization of Retardation Time Maps—So far, we have shown how the compression device can be used to measure the retardation time of the material based on surface displacement. Figure 5 and Table 1 show the results of overall retardation time measurements.

Here, we apply the same process on the strain profile of each point within the phantom (Fig. 8) to calculate the retardation times T_1 and T_2 maps. Figure 9 shows the resulting T_1 and T_2 maps.

The average values for these two maps in this figure are 3.4 seconds and 33.6 seconds for T_1 and T_2, respectively. The related strain for T_1 part, ε_1, is around 2 % and for T_2 part, ε_2, is around 3 %. It is also noted that compared to the strain map in Fig. 8(a), the retardation time maps in Fig. 9 show a relatively uniform distribution with only few scattered variations.

Figure 10 shows the fit error estimation map of the second order Kelvin-Voigt model, Eq.5. This map was made using equation (7). As it can be seen, the error is mostly less than 2%, which confirms the suitability of the second-order Kelvin–Voigt model as well as the overall strain tracking performance.

To explore the reproducibility of the results, this experiment was repeated 5 times on the same phantom with the same force, 3 N, and the ramp speed of 18 N/s. There was a five-minute resting time between each trial and the sample was not removed or repositioned for these five trials. No sign of damage was observed in phantom while performing the test.

Table 2 shows the T_1 and T_2 values in 5 trials on the same homogenous phantom using the same force and ramp speed.

The average T_1 and T_2 values measured with the Bose instrument were 3.4 seconds and 38 seconds, respectively. Comparing these values with those values measured by ultrasound and the average values of T_1 and T_2 map is reported in Table 2. The resulting relative errors for T_1 and T_2 are 5.9 % and −13.1%, respectively.

G. Inclusion phantom—To demonstrate the performance of the device on media with different sizes and stiffness values, we built two uniform cubic phantoms: A (softer) and B (stiffer). We created a third inclusion phantom in which the background material was similar to the phantom A, and contained a cylindrical inclusion that was made from the same material as the one used in phantom B.

The dimensions of the uniform phantoms A and B are 7.5 cm × 5.5 cm × 2 cm (L × W × H). The inclusion phantom dimensions are 7.5cm × 5.5cm × 5.5 cm (L × W × H), with the cylindrical inclusion having a 1.5 cm diameter.

To make phantom A(softer) we used 32.3 grams gelatin (Sigma-Aldrich, St. Louis, MO), 30 ml Vanicream Lite (Pharmaceutical Specialties, Inc., Rochester, MN), 6 grams cellulose (Sigma-Aldrich) for ultrasound scattering, and 6 grams potassium sorbate (Sigma-Aldrich) as a preservative, dissolved in enough distilled water to make the total solution volume equal 600 ml. Phantom B (stiffer) was made of 25.14 grams of gelatin (Sigma-Aldrich; St. Louis, MO); 60 ml propylene glycol (Sigma-Aldrich, St. Louis, MO); and 4 grams cellulose (Sigma-Aldrich) for ultrasound scattering, dissolved in enough distilled water to make the total solution volume equal 300 ml.

First, the uniform phantom A and the background part of the inclusion phantom were made and then the day after phantom B and inclusion part of inclusion phantom were made. The phantoms were kept at room temperature for a day before using them in the experiments.

To measure the dynamic response of the medium, we used the compression device to apply 8 N force with 16 N/s ramp on each of the phantoms. The ultrasound frame rate was 20 Hz during the acquisition time of 20 seconds. Thus, 400 frames were acquired for each experiment. Two initial seconds of data was removed.

In order to reduce memory needs and processing time for the inclusion phantom experiment, we processed approximately 3 cm of B-mode images in the axial and lateral direction, and for the uniform cubic phantoms, we processed only 1.5 cm of B-mode images in the axial direction. All of these experiments were done at room temperature.

The B-mode image of the stiff phantom B is shown in Fig. 11(a). The strain profiles of four points specified in Fig. 11(a) is demonstrated in Fig. 11(b). These strain profiles are normalized and shown in part (c) of this figure, which shows the material has essentially the same behavior at these points. In Fig. 11(d) the strain profiles of point1 and point 2 accompanied with standard deviation are shown.

As explained in the previous section, acquiring the strain profile can be used to measure the retardation time, T_1, for each strain profile.

As it was shown in previous part of this paper the T_2 value for gelatin phantom is more than 30 seconds. Since, for this part, we recorded only 20 seconds of data, therefore a single exponential, Eq. (9), is used to fit to the strain profiles at each spatial location to construct the T_1 value map.

$$\varepsilon(t)=\varepsilon_1(1-\exp(-\frac{t}{T_1})) \quad (9)$$

In Fig. 12(b), the measured T_1 value is 7.3±0.5 seconds while the fitting error map for this area is less than 2% as shown in Fig. 12(c). The same procedure was done for phantom A and the inclusion phantom. Figure 13 shows the resulting maps. The T_1 value measured for phantom A shown in Fig. 13(b) is 6.2 ± 0.4 seconds.

We tested the performance of compression device also on the inclusion phantom with different size and structure, non-uniform phantom, comparing to previous phantoms. To construct the T_1 map of inclusion phantom, Eq. (9) was used in the similar way that was used for both uniform phantoms A and B. The B-mode image of inclusion phantom and the strain profile of several specific points in this figure are illustrated in

Figure 15 shows the strain, T_1 map and the fitting error map for the inclusion phantom. The maps in this figure show the outcome of the creep response after removing the initial 2 seconds of data. The fitting error shown in Fig. 15(c) is less than 4% for this inclusion phantom.

As it was explained the calculated T_1 value for uniform phantom B or stiffer one was 7.3 ± 0.5 seconds and for the inclusion part of the inclusion phantom was 7.1 ± 0.8. In the same way for uniform phantom A or softer one, the calculated T_1 value is 6.2 ± 0.4 seconds and for back ground part of the inclusion phantom was 5.9 ± 0.3 seconds.

The relative error of phantom B, stiffer uniform phantom, and inclusion part of inclusion phantom is 2.7 % and for its background and soft uniform phantom, phantom A, 4%.

IV. Discussion

The goal of designing the automated compression device was to apply a prescribed amount of force for a predetermined time on a phantom or tissue to study its creep response during a period of time. A potential future application is to use this device for imaging the viscoelasticity of breast tissue or other organs in a group of patients. One of the important elements in this device is the combination of back plate that includes four sensors, located symmetrically at four corners of this plate, and pressure plate that is in contact with the other side of the sensors. Outputs of these sensors are summed, thus these sensors collectively measure the total applied force that is applied to the object by the pressure plate. Therefore, even in cases where the compression plate is not able to make complete contact with the surface of the object, for example, when the object's surface is not completely flat, the sensors can still measure the total force applied to the contact surface. This feature also increases the flexibility of device application on tissues with curved surface like breast because in such cases the pressure may not be evenly distributed. The device ability to measure the surface displacement is another important feature. The surface displacement profile helps to validate this compression device when comparing to a standard mechanical

testing machine. To validate the compression device, the Bose instrument was used for comparison.

Gelatin is an appropriate model to study the viscoelastic properties of breast tissue because of its similarity to breast stroma [10]. In both cases, the mechanical properties are established by a high molecular-weight, type I collagen matrix that is saturated in water [10]. In this paper, we used three different phantoms and one with inclusion. All phantoms are based on gelatin.

The results showed strong agreements between the two devices, the automated compression device and the Bose system, with an average relative error of 2.9% and 12.4%, for T_1 and T_2, respectively, based on surface displacement measured by these two devices. It is understood that, in general, the strain on the surface and inside the phantom are not necessarily the same. However, our investigation to measure retardation times for each point inside the same phantom by ultrasound reveal a good agreement between the surface and internal computed retardation time constants, where the error was less than 15 %.

We also showed that the measured retardation times T_1 and T_2 across a uniform phantom resulted in 2D maps, as shown in Figure 9. These results suggest that T_1 and T_2 maps are less sensitive to the geometry and boundary condition variations than the strain map (Figure 8(a)). There are some large regional variation in T_1 and T_2 maps. However, the area of these regions is small compared to the total area of the image. This can be verified by calculating the mean and standard deviation of the maps, which are 3.4±0.13 s for T_1 map and 33.6±1.25 s for T_2 map.

Appropriateness of a second order Kelvin-Voigt model was tested. Figure 10 showed that the fitting error was less than 2% in most of the region across the phantom. Repeatability tests also showed that the retardation times could be measured with small variations in measurement results.

For the repeatability check, the creep test was repeated five times on the phantom. The resulting relative errors for T_1 and T_2 are 2.9 % and 12.4%, respectively, showing a reasonable repeatability of the test.

To test the performance of the device for different media with different stiffness and sizes, we used three different gelatin phantoms. The error fit for all the cases was less than 5%. The relative error related to T_1 values for the part made with same material but in different shapes was small, i.e., less than 5%.

In the first uniform phantom study the data was recorded for 85 seconds. Thus it was possible to use a double exponential to calculate the T_2 value, which is usually is more than 30 seconds for that phantom. In medical applications, and especially for the breast (which is the future goal of this study), however, the recording time is often limited to the time the patient can hold her breath, which is usually less than 20 seconds. Keeping this in mind, we limited the recording time to 20 seconds in the latter part of the paper. In these experiments, it was not necessary to use a double exponential due to the shorter recording time, thus a single exponential was applied. In both cases the error fit is less than 5 %.

A potential source for different appearances of the retardation time map in Figures 12 and 13 compared to that in Figure 9 is that we used different recipes for the phantoms used in those two sets of experiments. Another potential source could be damage to the phantoms due to multiple compressions applied to the phantoms during the experiments. Similar experimental variables could be responsible for the different appearances of the strain profiles in Figures 8 and 14. These variations are some of the issues that we plan to explore in more details in our future studies.

It should be noted that all of the processing have been done offline and the total computation time was less than 3 minutes.

One of the limitations of the compression device, and generally this method, is restrictions in accessing internal organs for measuring the creep response. Due to that limitation, organs with easy access, such as the breast, thyroid, and possibly prostate are the best candidates for this method. Another limitation of this method is in the way the data is recorded. Although particle displacement measurement by ultrasound is very accurate, it only measures the axial displacement. Displacement measurement in other dimensions is not as accurate with conventional ultrasound imaging.

As we mentioned before, creep test has been done on a small group of patients with nonpalpable breast masses to differentiate between the benign and malignant masses [51]. However that study was performed with manual compression of the probe onto the breast. The present compression device provides a means for conducting the creep test in a more objective way with improved control of the applied compression compared to manual compression.

The creep test method described in this paper is particularly suitable for evaluation of breast masses. Elastography methods that are currently used in clinics for breast evaluation are primarily designed to measure the stiffness of breast masses. The creep test method described here provides information on viscosity as well as elasticity. The additional information would improve differentiation of mass pathology and thus may have a significant impact on breast cancer diagnosis.

Future work will include using the automated compression device described here to measure the retardation time in human (e.g., in breast) for diagnostic purposes.

V. Conclusion

In this paper we described the design of a device for applying an approximate step force on a tissue-mimicking phantom and measuring the creep response using an ultrasound probe. Retardation time was calculated by fitting a second order Kelvin-Voigt model to the displacement and strain profiles obtained from the device. The performance of the device was validated through a series of creep tests on a phantom and comparing the resulting retardation times with those from a standard mechanical testing instrument. Beside that its performance was also checked on phantoms with different size and stiffness by applying first order Kelvin-Voigt model. The overall results of this work justify the suitability of this device for performing creep tests on tissue-like materials.

Acknowledgments

This work was supported by grant R01CA168575 from the National Cancer Institute (NCI) and the National Institutes of Health (NIH). The content is solely the responsibility of the authors and does not necessarily represent the official views of NCI or NIH.

We thank Mr. Lawrence Berglund from Mayo Clinic Biomechanics Laboratory for experimental assistance with the Bose instrument.

References

1. Hoffler CE, Guo XE, Zysset PK, Goldstein SA. An application of nanoindentation technique to measure bone tissue Lamellae properties. J Biomech Eng. 2005 Dec; 127(7):1046–53. [PubMed: 16502646]
2. Oyen ML. Nanoindentation of biological and biomimetic materials. Experimental Techniques. 2011; 37:73–87.
3. Fei, Liu, Daniel, J. Tschumperlin, Micromechanical characterization of lung tissue using atomic force microscopy. J Vis Exp. 2011 Aug 28.(54)
4. Ulrich TA, Jain A, Tanner K, MacKay JL, Kumar S. Probing cellular mechanobiology in three-dimensional culture with collagen agarose matrices. Biomaterials. 2010; 31:1875–1884. [PubMed: 19926126]
5. Rao RR, Peterson AW, Ceccarelli J, Putnam AJ, Stegemann JP. Matrix composition regulates three-dimensional network formation by endothelial cells and mesenchymal stem cells in collagen/fibrin materials. Angiogenesis. 2012; 15:253–264. [PubMed: 22382584]
6. Svensson A, Nicklasson E, Harrah T, Panilaitis B, Kaplan D, Brittberg M, Gatenholm P. Bacterial cellulose as a potential scaffold for tissue engineering of cartilage. Biomaterials. 2005; 26:419–431. [PubMed: 15275816]
7. Rowe SL, Lee S, Stegemann JP. Influence of thrombin concentration on the mechanical and morphological properties of cell-seeded fibrin hydrogels. Actabiomaterialia. 2007; 3:59–67.
8. Liu KK, Ju BF. A novel technique for mechanical characterization of thin elastomeric membrane. Journal of Physics D: Applied Physics. 2001; 34:L91.
9. Tsakalakos T. The bulge test: a comparison of the Theory and experiment for isotropic and anisotropic films. Thin solid films. 1981; 75:293–305.
10. Ophir J, Céspedes I, Ponnekanti H, Yazdi Y, Li X. Elastography: a quantitative method for imaging the elasticity of biological tissues. Ultrasonic Imaging. 1991; 13(2):111–134. [PubMed: 1858217]
11. Sarvazyan AP, Rudenko OV, Swanson SD, Fowlkes JB, Emelianov SY. Shear wave elasticity imaging: a new ultrasonic technology of medical diagnostics. Ultrasound in medicine & biology. 1998; 24:1419–1435. [PubMed: 10385964]
12. Muthupillai R, Lomas D, Rossman P, Greenleaf JF. Magnetic resonance elastography by direct visualization of propagating acoustic strain waves. Science. 1995; 269:1854. [PubMed: 7569924]
13. Bercoff J, Tanter M, Fink M. Supersonic shear imaging: a new technique for soft tissue elasticity mapping. Ultrasonics, Ferroelectrics, and Frequency Control, IEEE Transactions on. 2004; 51:396–409.
14. Nightingale K, McAleavey S, Trahey G. Shear-wave generation using acoustic radiation force: In vivo and ex vivo results. Ultrasound Med Biol. Dec.2003 29:1715–23. [PubMed: 14698339]
15. Hong X, Stegemann JP, Deng CX. Microscale characterization of the viscoelastic properties of hydrogel biomaterials using dual-mode ultrasound elastography. Biomaterials. 2016; 88:12–24. [PubMed: 26928595]
16. Catheline S, Thomas JL, Wu F, Fink MA. Diffraction field of a low frequency vibrator in soft tissues using transient elastography. Ultrasonics, Ferroelectrics, and Frequency Control, IEEE Transactions on. 1999; 46:1013–1019.
17. Chen S, et al. Shearwave dispersion ultrasound vibrometry (SDUV) for measuring tissue elasticity and viscosity. Ultrasonics, Ferroelectrics, and Frequency Control, IEEE Transactions on. 2009; 56(1):55–62.

18. Sandrin L, Fourquet B, Hasquenoph JM, Yon S, Fournier C, Mal F, Christidis C, Ziol M, Poulet B, Kazemi F, Beaugrand M, Palau R. Transient Elastography: A new noninvasive method for assessment of hepatic fibrosis. Ultrasound Med Biol. 2003 Dec; 29(12):1705–13. [PubMed: 14698338]
19. Bavu E, Gennisson JL, Couade M, Bercoff J, Mallet V, Fink M, Badel A, Vallet-Pichard A, Nalpas B, Tanter M, Pol S. Noninvasive in vivo liver fibrosis evaluation using supersonic shear imaging: a clinical study on 113 hepatitis C virus patients. Ultrasound Med Biol. 2011 Sep; 37(9):1361–73. [PubMed: 21775051]
20. Tanter M, Bercoff J, Athanasiou A, Deffieux T, Gennisson JL, Montaldo G, Muller M, Tardivon A, Fink M. Quantitative assessment of breast lesion viscoelasticity: initial clinical results using supersonic shear imaging. Ultrasound Med Biol. 2008 Sep; 34(9):1373–86. [PubMed: 18395961]
21. Denis M, Mehrmohammadi M, Song P, Meixner DD, Fazzio RT, Pruthi S, Whaley DH, Chen S, Fatemi M, Alizad A. Comb-push ultrasound shear elastography of breast masses: Initial results show promise. PloS one. 2015; 10:e0119398. [PubMed: 25774978]
22. Bhatia KS, Tong CS, Cho CC, Yuen EH, Lee YY, Ahuja AT. Shear wave elastography of thyroid nodules in routine clinical practice: preliminary observations and utility for detecting malignancy. EurRadiol. 2012 Nov; 22(11):2397–406.
23. Mehrmohammadi M, Denis M, Song P, Chen S, Fatemi M, Alizad A. Comb-Push Ultrasound Shear Elastography of thyroid: Preliminary in vivo human study. Ultrasonics Symposium (IUS), 2014 IEEE International. 2014:213–216.
24. Palmeri ML, Glass TJ, Miller ZA, Rosenzweig SJ, Buck A, Polascik TJ, Gupta RT, Brown AF, Madden J, Nightingale KR. Identifying Clinically Significant Prostate Cancers using 3-D In Vivo Acoustic Radiation Force Impulse Imaging with Whole-Mount Histology Validation. Ultrasound in medicine & biology. 2016; 42:1251–1262. [PubMed: 26947445]
25. Sinkus R, Tanter M, Catheline S, Lorenzen J, Kuhl C, Sondermann E, Fink M. Imaging anisotropic and Viscous properties of breast tissue by magnetic resonance-elastography. Magnetic resonance in medicine. 2005; 53:372–387. [PubMed: 15678538]
26. Deffieux T, Montaldo G, Tanter M, Fink M. Shear wave spectroscopy for in vivo quantification of human soft tissues visco-elasticity. Medical Imaging, IEEE Transactions on. 2009; 28:313–322.
27. Chaturvedi P, Insana MF, Hall TJ. 2-D Companding for noise reduction in strain imaging. IEEE Transactions on Ultrasonics Ferroelectrics and Frequency Control. 1998; 45(1):179–91.
28. Garra BS, Cespedes EI, Ophir J, Spratt SR, Zuurbier RA, Magnant CM, Pennanen MF. Elastography of breast lesions: initial Clinical results. Radiology. 1997; 202:79–86. [PubMed: 8988195]
29. Burnside ES, Hall TJ, Sommer AM, Hesley GK, Sisney GA, Svensson WE, Fine JP, Jiang J, Hangiandreou NJ. Differentiating benign from malignant solid breast masses with US strain imaging 1. Radiology. 2007; 245:401–410. [PubMed: 17940302]
30. Itoh A, Ueno E, Tohno E, Kamma H, Takahashi H, Shiina T, Yamakawa M, Matsumura T. Breast disease: clinical application of US elastography for diagnosis. Radiology. 2006 May; 239(2):341–50. [PubMed: 16484352]
31. Pallwein L, Mitterberger M, Struve P, Pinggera G, Horninger W, Bartsch G, Aigner F, Lorenz A, Pedross F, Frauscher F. Real-time elastography for detecting prostate cancer: preliminary experience. BJU Int. 2007 Jul.100(1):4.
32. Lyshchik A, Higashi T, Asato R, Tanaka S, Ito J, Mai JJ, Pellot-Barakat C, Insana MF, Brill AB, Saga T. Thyroid gland tumor diagnosis at US elastography1. Radiology. 2005; 237:202–211. [PubMed: 16118150]
33. Banks HT, Hu S, Kenz ZR. A brief review of elasticity and viscoelasticity for solids. Advances in Applied Mathematics and Mechanics. 2011; 3:1–51.
34. Orescanin M, Qayyum MA, Toohey KS, Insana MF. Dispersion and shear modulus measurements of porcine liver. Ultrasonic Imaging. 2010; 32(4):255–66. [PubMed: 21213570]
35. Hoyt K, Castaneda B, Zhang M, Nigwekar P, di Sant'agnese PA, Joseph JV, Strang J, Rubens DJ, Parker KJ. Tissue elasticity properties as biomarkers for prostate cancer. Cancer Biomark. 2008; 4(4–5):213–25. [PubMed: 18957712]

36. Kiss MZ, Varghese T, Hall TJ. Viscoelastic characterization of in vitro canine tissue. Phys Med Biol. 2004; 49(18):4207–18. [PubMed: 15509061]
37. Sloninsky GL. Laws of mechanical relaxation processes in polymers. J Polym Sci, Part C. 1967; 16:1667–1672.
38. Coussot C, Kalyanam S, Yapp R, Insana MF. Fractional derivative models for ultrasonic characterization of polymer and breast tissue viscoelasticity. Ultrasonics, Ferroelectrics, and Frequency Control, IEEE Transactions on. 2009; 56:715–726.
39. Huwart, Peeters F, Sinkus R, Annet L, Salameh N, terBeek LC, Horsmans Y, Van Beers BE. Liver fibrosis: non-invasive assessment with MR elastography. NMR Biomed. 2006; 19:173–9. [PubMed: 16521091]
40. Chen S, Sanchez W, Callstrom MR, Gorman B, Lewis JT, Sanderson SO, Greenleaf JF, Xie H, Shi Y, Pashley M, Shamdasani V, Lachman M, Metz S. " Assessment of liver viscoelasticity by using shearwaves induced by ultrasound radiationforce. Radiology. 2013; 266:964–970. [PubMed: 23220900]
41. Insana MF, Pellot-Barakat C, Sridhar M, Lindfors KK. Viscoelastic imaging of breast tumor microenvironment with ultrasound. journal of mammary gland biology and neoplasia. 2004; 9:393–404. [PubMed: 15838608]
42. Sridhar M, Liu J, Insana M. Viscoelasticity imaging using ultrasound: parameters and error analysis. Physics in medicine and biology. 52:2425.
43. Losa GA, Alini M. Sulfated proteoglycans in the extracellular matrix of human breast tissues with infiltrating carcinoma. International journal of cancer. 1993; 54:552557.Biomechanical Engineering. 2009; 131:081005.
44. Sridhar M, Liu J, Insana M. Viscoelasticity imaging using ultrasound: parameters and error analysis. Physics in medicine and biology. 2007; 52:2425. [PubMed: 17440244]
45. Ebihara T, Venkatesan N, Tanaka R, Ludwig M. Changes in extracellular matrix and tissue viscoelasticity in bleomycin induced lung fibrosis. Am J Respir Crit Care Med. 2000; 162:1569–1576. [PubMed: 11029378]
46. Garteiser P, Doblas S, Daire JL, Wagner M, Leitao H, Vilgrain V, Sinkus R, Van Beers BE. MR elastography of liver tumours: value of viscoelastic properties for tumour characterisation. Eur Radiol. 2012; 22:2169–2177. [PubMed: 22572989]
47. Phipps S, Yang TH, Habib FK, Reuben RL, McNeill SA. Measurement of The mechanical characteristics of benign prostatic tissue: a novel method for assessing benign prostatic disease. Urology. 2005; 65:1024–1028. [PubMed: 15882757]
48. Xu, F., Wen, T., Seffen, KA., Lu, TJ. Characterization of thermomechanical behaviour of skin tissue II. Viscoelastic Behaviour, World Congress on Engineering 2007 V; London. 2007.
49. Omari EA, Varghese T, Kliewer MA, Harter J, Hartenbach EM. Dynamic and quasi-static mechanical testing for characterization of the viscoelastic properties of human uterine tissue. Journal of biomechanics. 2015; 48:1730–1736. [PubMed: 26072212]
50. Sridhar M, Insana MF. Ultrasonic Measurements of breast viscoelasticity. Medical physics. 2007; 34:4757–4767. [PubMed: 18196803]
51. Qiu Y, Sridhar M, Tsou JK, Lindfors KK, Insana MF. Ultrasonic viscoelasticity imaging of nonpalpable breast tumors: preliminary results. Academic radiology. 2008; 15:1526–1533. [PubMed: 19000869]
52. Palacio-Torralba J, Hammer S, Good DW, McNeill SA, Stewart GD, Reuben RL, Chen Y. Quantitative diagnostics of soft tissue through viscoelastic characterization using time-based instrumented palpation. Journal of the mechanical behavior of biomedical materials. 2015; 41:149–160. [PubMed: 25460411]
53. Chan D, Neu C, Hull M. In situ deformation of cartilage in cyclically loaded tibiofemoral joints by displacement-encoded MRI. Osteoarthritis and Cartilage. 2009; 17:1461–1468. [PubMed: 19447213]
54. Campana S, Charpail E, De Guise J, Rillardon L, Skalli W, Mitton D. Relationships between viscoelastic properties of lumbar intervertebral disc and degeneration grade assessed by MRI. Journal of the mechanical behavior of biomedical materials. 2011; 4:593–599. [PubMed: 21396608]

55. Bamber JC, Bush NL. Freehand elasticity imaging using speckle decorrelation rate. Acoustical imaging: Springer. 1996:285–292.
56. Varghese T, Zagzebski J, Frank G, Madsen E. Elastographic imaging using a Handheld compressor. Ultrasonic imaging. 2002; 24:25–35. [PubMed: 12102226]
57. Hiltawsky KM, Kruger M, Starke C, Heuser L, Ermert H, Jensen A. Springer, editor. Freehand Ultrasound elastography of breast lesions: clinical results. Acoustical imaging. 2001; 27:1461–1469. 1996.
58. Hall TJ, Bilgen M, Insana MF, Krouskop TA. Phantom materials for elastography. Ultrasonics Ferroelectrics and Frequency Control, IEEE Transactions. 1997; 44:1355–1365.
59. Lorenz A, Sommerfeld HJ, Garcia-Schurmann M, Philippou S, Senge T, Ermert H. A new system for the acquisition of ultrasonic multi compression strain Images of the human prostate in vivo. Ultrasonics Ferroelectrics and Frequency Control, IEEE Transactions on. 1999; 46:1147–1154.
60. Coutts L, Bamber J, Miller N, Mortimer P. Ultrasound elastography of the Skin and Subcutisunder surface extensive loading. Ultrasound. 2006; 14:161–166.
61. Gilbertson, MW., Anthony, BW. Ergonomic control strategies for a handheld force-Controlled ultrasound probe. Intelligent Robots and Systems(IROS), 2012 IEEE/RSJ International Conference on; 2012. p. 1284-1291.
62. Fortin M, Buschmann MD, Bertrand MJ, Foster FS, Ophir J. Cross-Correlation of ultrasound A-lines to obtain Dynamic displacement profiles within Poroelastic materials undergoing stress relaxation. Medical Imaging. 2000
63. Righetti R, Ophir J, Srinivasan S, Krouskop TA. The feasibility of using elastography for imaging the Poisson's ratio in porous media. Ultrasound Med Biol. 2004 Feb; 30(2):215–28. [PubMed: 14998674]
64. Nair SP, Yang X, Krouskop TA, Righetti R. Performance analysis of a new real-Time elastographic time constant estimator. Medical Imaging, IEEE Transactions on. 2011; 30:497–511.
65. Nair S, Varghese J, Chaudhry A, Righetti R. Effect of temporal acquisition parameters on image quality of strain time constant elastography. Ultrasonic imaging. 2014 0161734614539665.
66. Amador C, Kinnick RR, Urban MW, Fatemi M, Greenleaf JF. Viscoelastic Tissue mimicking phantom validation study with shear wave elasticity imaging and viscoelastic spectroscopy. Ultrasonics Symposium (IUS), 2015 IEEE International. 2015:1–4.
67. Yang, Y. PhD Thesis. BIOE Department, UIUC; Urbana, IL: Apr. 2016 Soft tissue viscoelastic properties: Measurements, models and interpretation.
68. Oyen ML. Spherical indentation creep following ramp loading. Journal of Materials Research. 2005; 20:2094–2100.
69. Aglyamov, SR., Park, S., Ilinskii, Y., Emelianov, SY. Ultrasound imaging of soft. tissue shear viscosity. Ultrasonics; IEEE Symposium on; 2003; 2003. p. 937-940.
70. Montaldo G, Tanter M, Bercoff J, Benech N, Fink M. Coherent plane-wave compounding for very high frame rate ultrasonography and transient elastography. IEEE Trans Ultrason Ferroelectr Freq Control. 2009; 56:489–506. [PubMed: 19411209]
71. Loupas T, Peterson RB, Gill RW. Experimental evaluation of velocity and power estimation for ultrasound blood-flow Imaging, by means of a 2-dimensional autocorrelation approach. IEEE Trans Ultrason Ferrorelectr Freq Control. 1995; 42:689–699.
72. Erkamp, R., Emelianov, S., Skovoroda, A., Chen, X., O'Donnell, M. Exploiting strain-hardening of tissue to increase contrast in elasticity imaging. Ultrasonics Symposium; 2000; IEEE; 2000. p. 1833-1836.
73. Erkamp RQ, Emelianov SY, Skovoroda AR, O'Donnell M. Nonlinear, elasticity imaging: theory and phantom study. Ultrasonics, Ferroelectrics, and Control, Frequency IEEE Transactions on. 2004; 51:532–539.
74. Eskandari H, Salcudean SE, Rohling R. Viscoelastic parameter estimation based on spectral analysis. Ultrasonics, Ferroelectrics, and Frequency Control, IEEE Transactions on. 2008; 55:1611–1625.
75. Ponnekanti H, Ophir J, Cespedes I. Axial stress distributions between coaxial compressors in elastography: an analytical model. Ultrasound in medicine& biology. 1992; 18:667–673. [PubMed: 1440988]

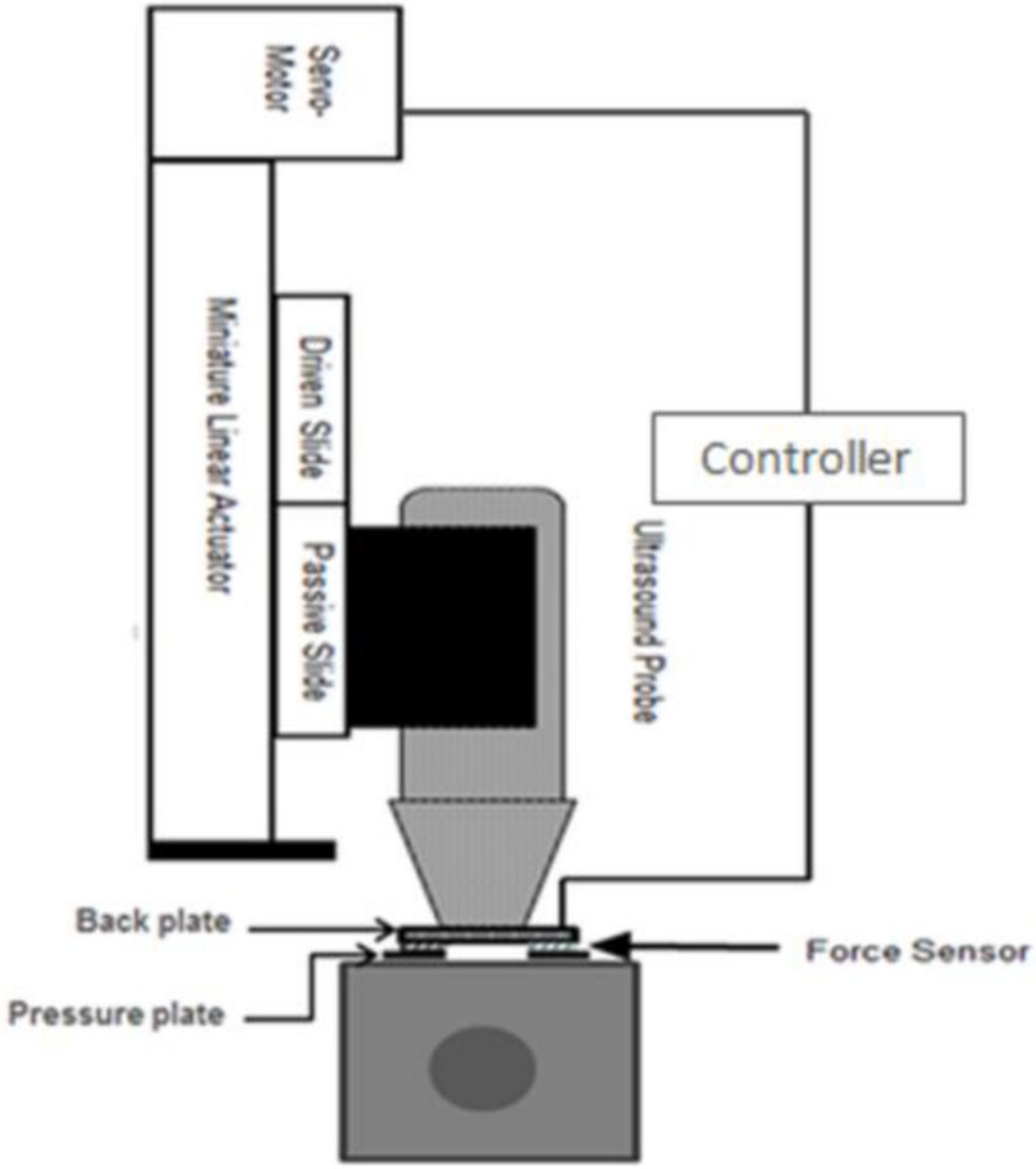

Figure 1.

Automated compression device. The device consists of an actuator, driven by servomotor, which moves an ultrasound probe rapidly into the material or tissue to be measured until a preset force level on the probe face is reached. The actuator control system uses small force sensors embedded in the back plate, attached to and surrounding the probe face to adjust the probe position as necessary to maintain the preset force level constant for a predetermined period of time. When the creep response measurement is complete, the actuator automatically retracts the probe.

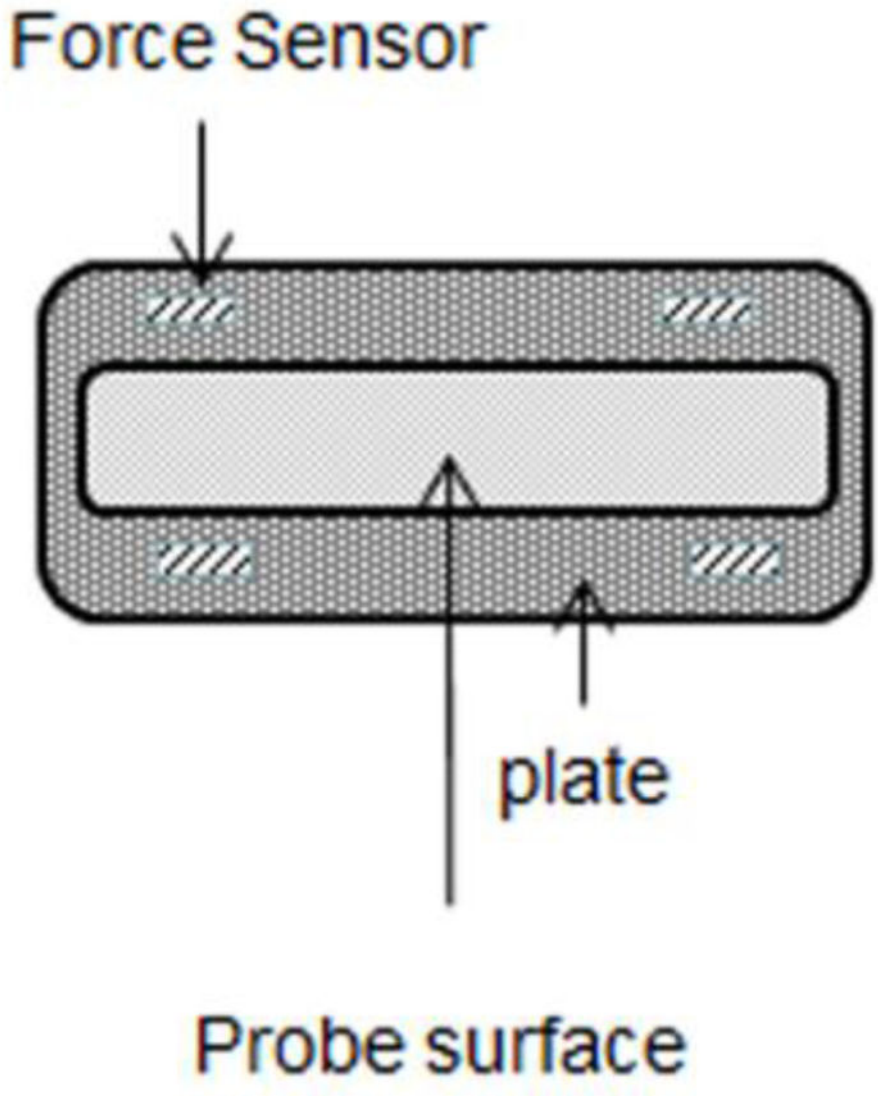

Figure 2.
This figure shows the probe surface and the pressure and back plates as well as 4 force sensors positioned at the 4 corners of the back plate. This figure also shows the front view including both pressure plate with membrane. The load cells are located between the pressuer plate and the back plate (not shown).

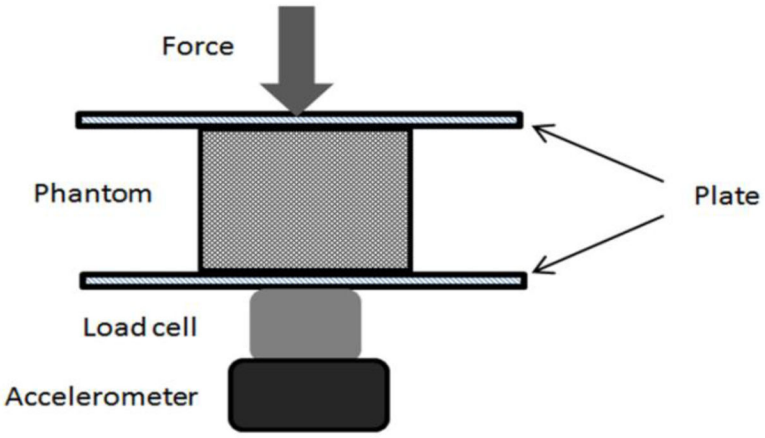

Figure 3.

Bose instrument block diagram including two plates with the force applied on top. There is a load cell at the bottom to measure the applied force and an accelerometer at the bottom of the load cell to compensate for the inertia.

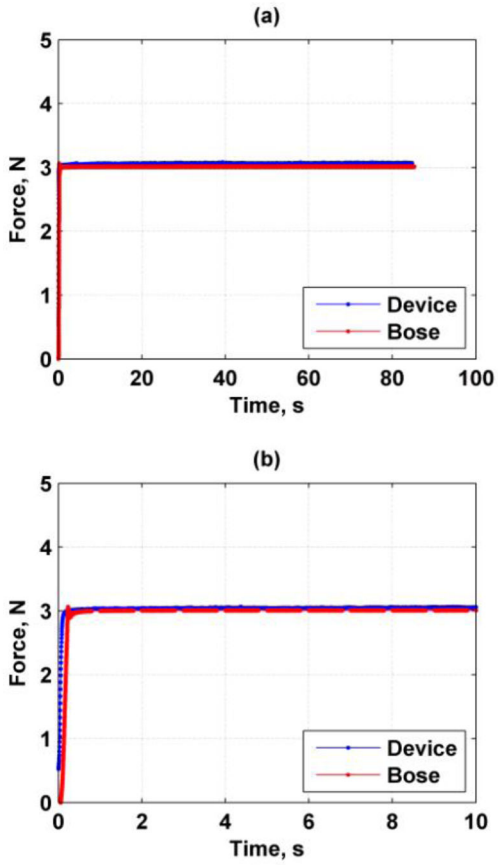

Figure 4.

Comparison of Bose instrument and compression device in generating 3 N force with 18 N/s ramp. The ramp part takes 0.17 seconds and after that the force remains constant for 85 seconds. (a) Force profile for the entire 85 sec (b) Force profile for the first 10 seconds presented for better visualization.

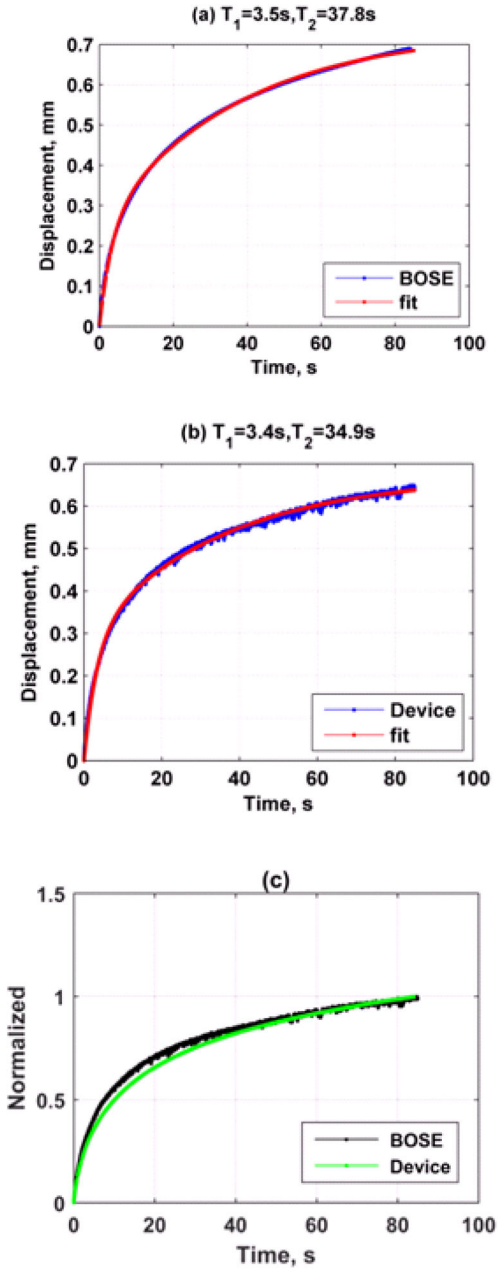

Figure 5.

Surface displacement profiles resulted from Bose instrument and the compression device. (a) Bose displacement profile and its fit with T_1= 3.5 seconds and T_2= 37.8 seconds value results. (b) Compression device displacement profile and its fit with T_1= 3.4 seconds and T_2= 34.9 seconds value results.(c) Bose and Device, normalized displacement profiles.

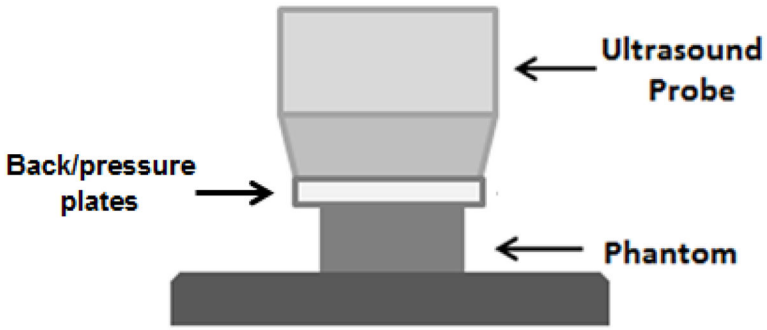

Figure 6.
Diagram showing the location of the probe, pressure/back plate and phantom located on a base.

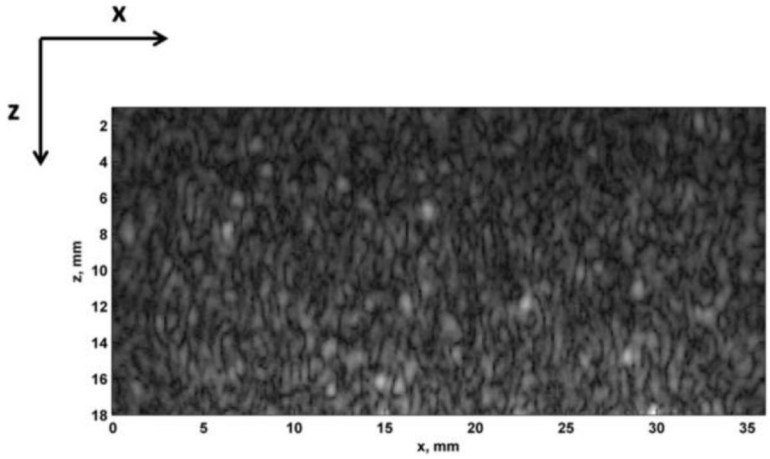

Figure 7.
B-mode image of the homogenous phantom.

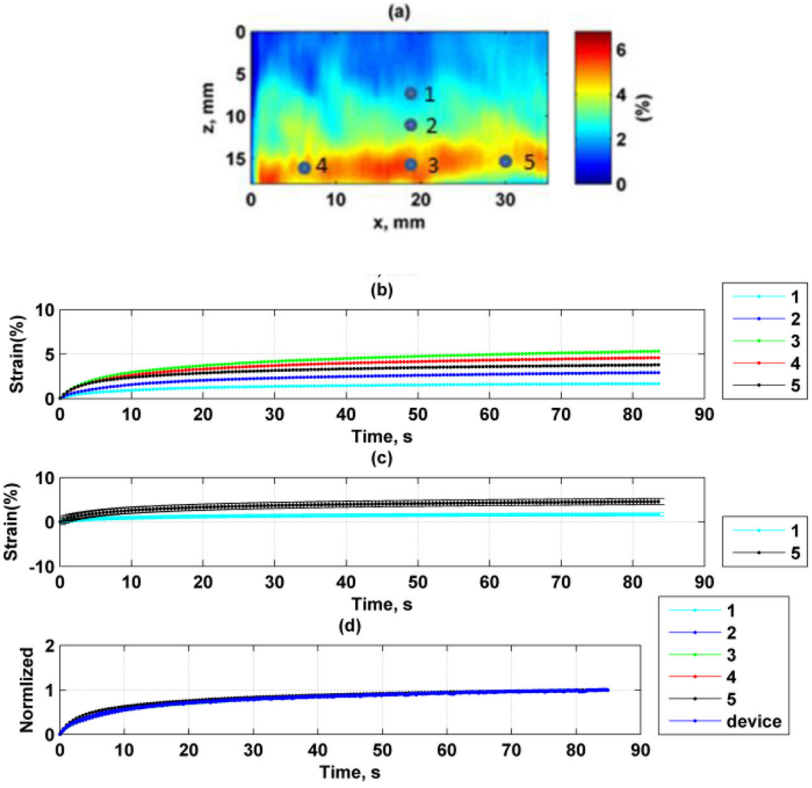

Figure 8.

Strain results. (a) Strain map (b) Strain profile for 85 seconds for 5 different spots specified in the strain map (a);(c) strain profiles of points 1 and 5 with standard deviation (d) Normalized surface displacement obtained directly from the compression device and the normalized versions of the strain profiles shown in (a).

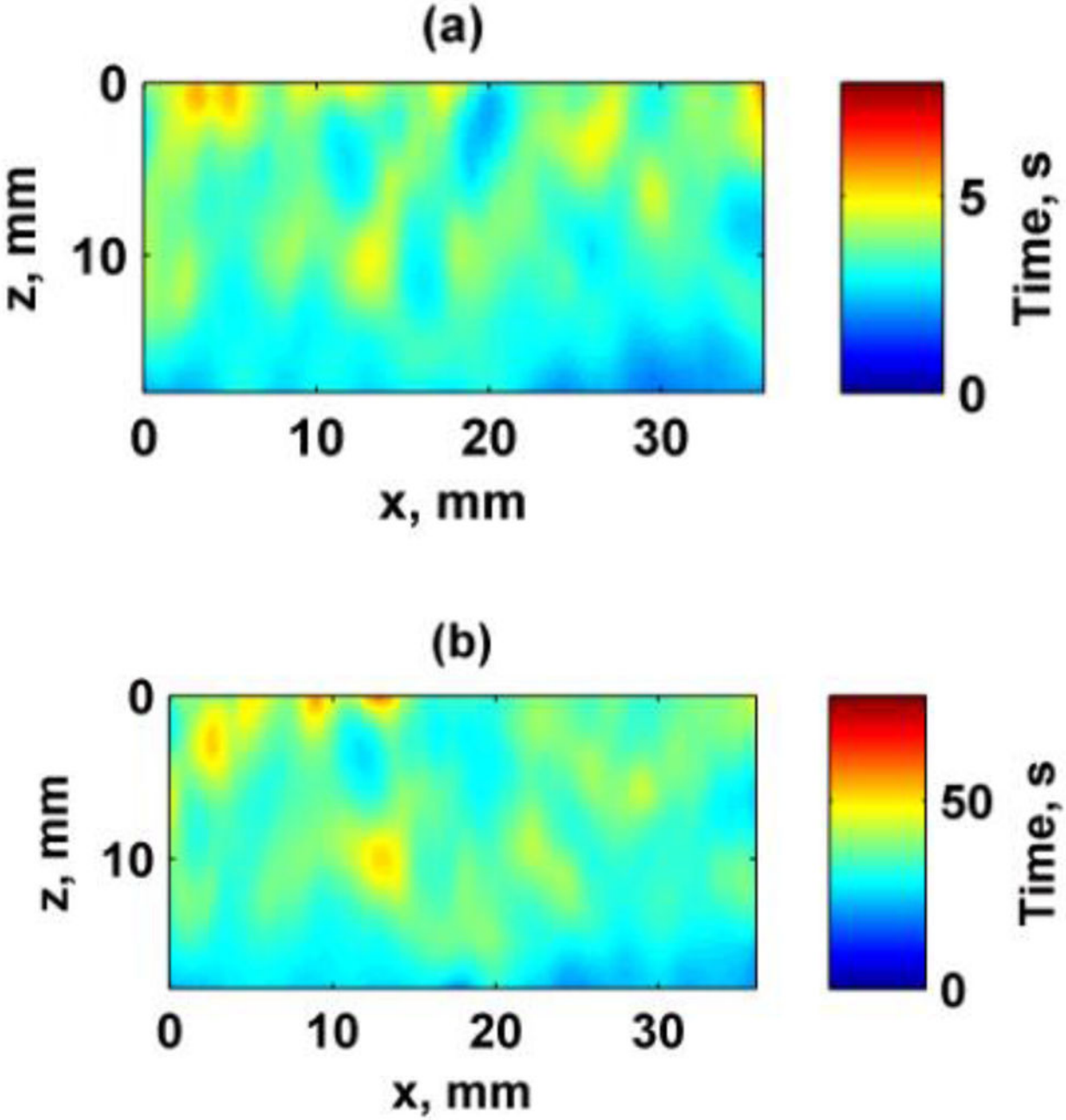

Figure 9.
Retardation times maps based on creep tests on a homogenous phantom. (a) T_1 map, 3.4±0.13 s; (b) T_2 map, 33.6±1.25 s

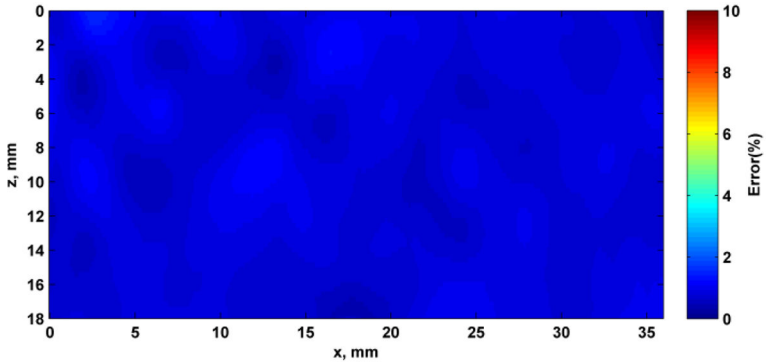

Figure 10.
Fitting error for homogenous phantom, 0.82±0.3 %

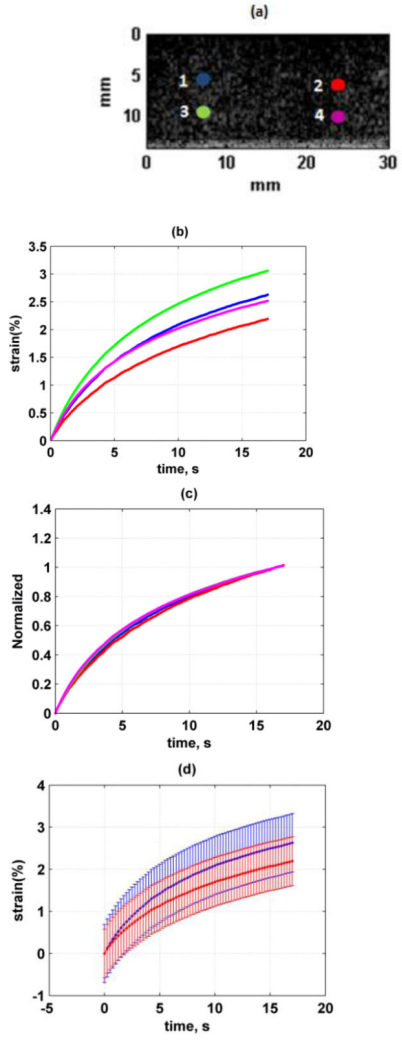

Figure 11.

(a) B-mode image of uniform B phantom, stiffer phantom. (b) Strain profiles of different specified points in B-mode image. (c) Normalized strain profile. (d) Strain profiles of points 1 and 2 accompanied with bars showing standard deviation.

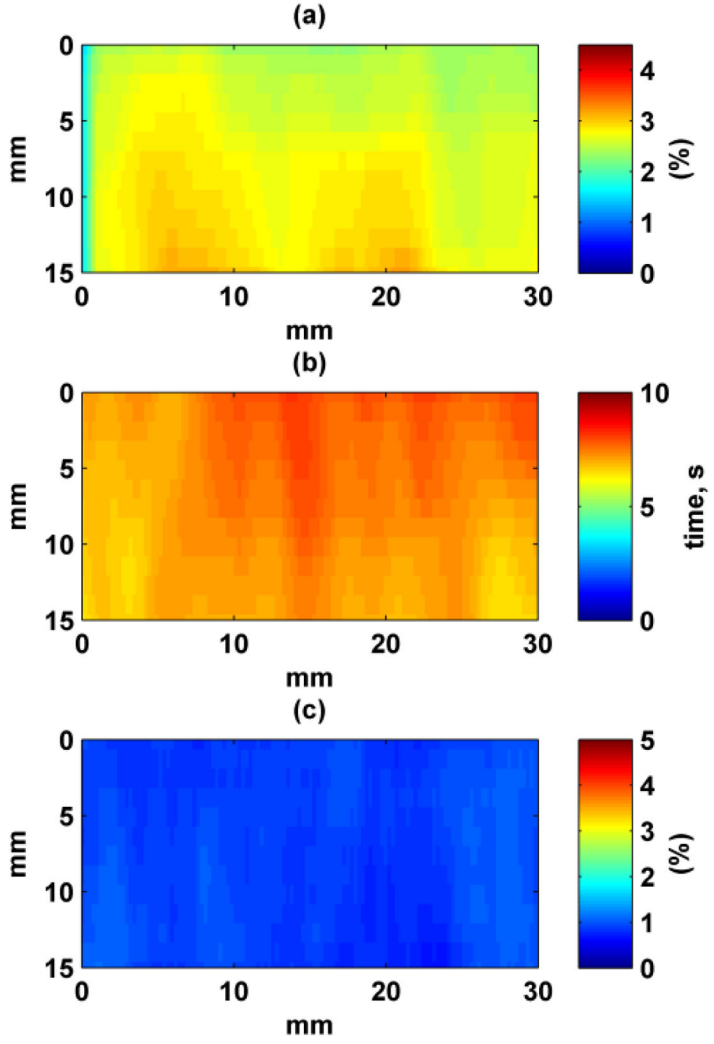

Figure 12.

Phantom B results.(a) Strain map of phantom B. (b) T_1 map of phantom B and the calculated mean T_1 value is 7.3 ± 0.5 seconds. (c) Fitting error map (0.86±0.043) %.

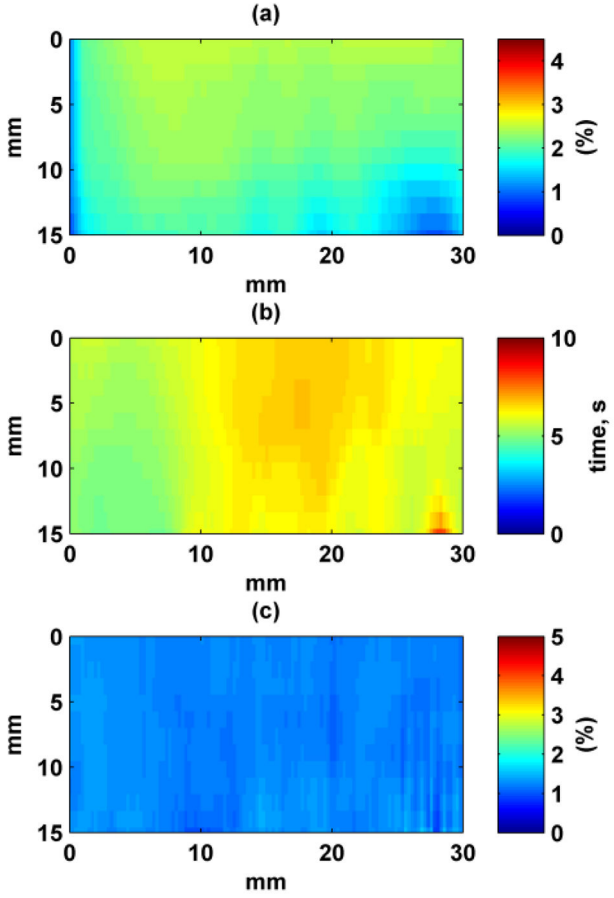

Figure 13.

Phantom A maps. (a) Strain map of phantom A. (b) T_1 map of phantom A. The calculated mean T_1value is 6.2 ± 0.4 seconds. (c) Fitting error map (1.25± 0.33) %.

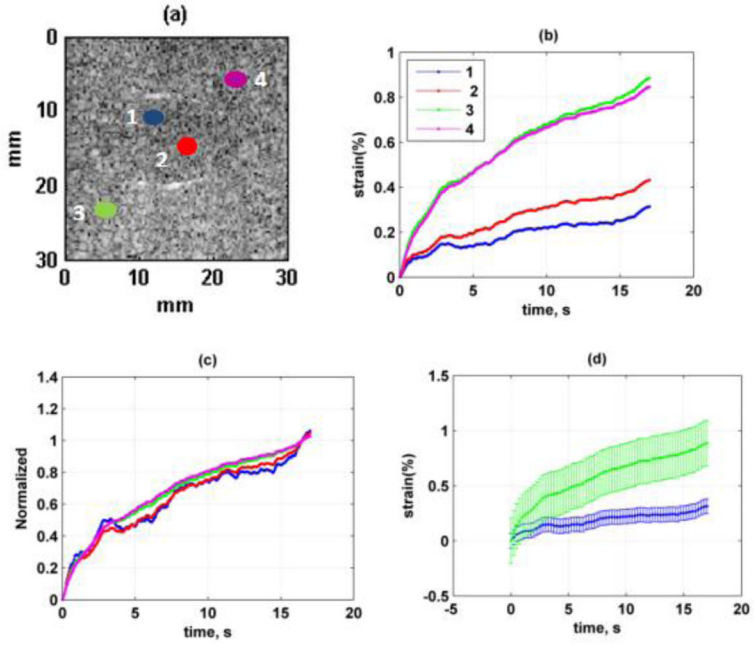

Figure 14.

B-mode and strain profiles. (a) Last B-mode image acquired in the experiment, (b) strain profiles of different locations specified in B-mode image, (c) normalized strain profiles accompanied with force after cutting two initial seconds.(d) Standard deviation of the strain profiles of point 1 and 3.

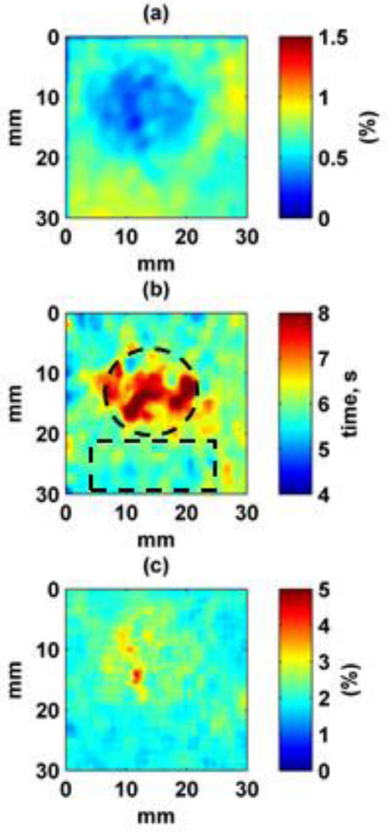

Figure 15.

Inclusion phantom. (a) Strain map of the inclusion phantom. (b) T_1 map of the inclusion phantom. The black dashed rectangular shows the area used for measuring the mean of T_1 value for the background material. The T_1 value for this area is 5.9 ± 0.3 seconds. The black circle shows the inclusion area. The mean of T_1 value inside inclusion area is 7.1 ± 0.8 seconds. (c) Fitting error map.

Table 1

Retardation time results for five trials on the same phantom with the same amount of force and ramp speed for both the compression device and Bose instrument.

Measurement method	Retardation times T_1 and T_2 in seconds						
	First	Second	Third	Fourth	Fifth	Average	Standard deviation
BOSE T_1 (s)	3.4	3.4	3.5	3.5	3.4	3.4	0.05
Device T_1 (s)	3.6	3.2	3.4	3.2	3.4	3.3	0.17
BOSE T_2 (s)	37.5	39.8	37.8	37.4	37.3	38	1.04
Device T_2 (s)	33.8	31.8	34.9	32.4	33.8	33.3	1.24

Table 2

T_1 and T_2 values

Measurement method	Retardation time, T_1 and T_2 in seconds						
	First	Second	Third	Fourth	Fifth	Mean	STD
US measurement: Mean T_1 (s)	3.7	3.6	3.4	3.7	3.6	3.6	0.12
BOSE T_1 (s)	3.4	3.4	3.5	3.5	3.4	3.4	0.05
US measurement: Mean T_2 (s)	32.4	32	33.6	33	34	33	0.74
BOSE T_2 (s)	37.5	39.8	37.8	37.4	37.3	38	1.04